Electrowetting-driven capacitance enhancement dependent on charge carrier and nanopore size

Eunji Lee[1], Jeonghun Lee[1], Dong Hyuk Kang[1], Jong Chan Hyun[1], Chan Yeol Kim[1], Jisoo Kim[1], Minho M. Kim[2], Beom Sik Youn[3], Juhee Yoon[4], Geunsu Bae[5], Kang Ho Shin[6], Sang Moon Lee[7], Ho Seok Park[6,8,9,10], Chang Hyuck Choi[5,11], Hyoung-Joon Jin[4,12], Hyung-Kyu Lim,[3,], Hyungjun Kim[2,*], Young Soo Yun[1,13,14,*]*

[1]*KU-KIST Graduate School of Converging Science and Technology, Korea University, 145 Anam-ro, Seongbuk-gu, Seoul 02841, Republic of Korea*

[2]*Department of Chemistry, Korea Advanced Institute of Science and Technology, 291 Daehak-ro, Yuseong-gu, Daejeon 34141, Republic of Korea*

[3]*Division of Chemical Engineering and Bioengineering, Kangwon National University, Chuncheon 24341, Republic of Korea*

[4]*Program in Environmental and Polymer Engineering, Inha University, Incheon 22212, Republic of Korea*

[5]*Department of Chemistry, Pohang University of Science and Technology (POSTECH), Pohang 37673, Republic of Korea*

[6]*School of Chemical Engineering, Sungkyunkwan University (SKKU), 2066, Seobu-ro, Jangan-gu, Suwon, Gyeonggi-do, 16419 Republic of Korea*

[7]*Division of Material Analysis and Research, Korea Basic Science Institute, Daejeon 34133, South Korea*

[8]*SKKU Institute of Energy Science and Technology (SIEST), Sungkyunkwan University (SKKU), 2066, Seobu-ro, Jangan-gu, Suwon, Gyeonggi-do, 16419 Republic of Korea*

[9]*SKKU Advanced Institute of Nano Technology (SAINT), Sungkyunkwan University (SKKU), 2066, Seobu-ro, Jangan-gu, Suwon, Gyeonggi-do, 16419 Republic of Korea*

[10]*Department of Health Sciences and Technology, Samsung Advanced Institute for Health Sciences and Technology (SAIHST), Sungkyunkwan University, 2066, Seobu-ro, Jangan-gu, Suwon, Gyeonggi-do, 16419 Republic of Korea*

[11]*Institute for Convergence Research and Education in Advanced Technology (I-CREATE), Yonsei University, Seoul 03722, Republic of Korea*

[12]*Department of Polymer Science and Engineering, Inha University, Incheon 22212, Republic of Korea*

[13]*Energy Storage Research Center, Korea Institute of Science and Technology (KIST), Hwarangro 14-gil 5, Seoungbuk-gu, Seoul, 02792, Republic of Korea*

[14]*Department of Integrative Energy Engineering, Korea University, 145 Anam-ro, Seongbuk-gu, Seoul 02841, Republic of Korea*

*Corresponding author.

Email: Y. S. Yun, c-ysyun@korea.ac.kr

H. kim, linus16@kaist.ac.kr

H.-K. Lim, hklim@kangwon.ac.kr

Abstract

Enhancing the specific capacitance of supercapacitors requires a deeper understanding of their charge storage mechanisms. While recent studies have primarily focused on micropore-dominant activated carbons (ACs) and monovalent ions, a more comprehensive and systematic exploration remains underexplored. In this work, we developed microporous and mesoporous AC electrodes with pore size distributions centered at 1.4 nm (AC14) and 3.7 nm (AC37), respectively. These electrodes were systematically evaluated in various electrolyte systems containing monovalent or multivalent cations and sulfate anions as charge carriers. A key finding of this study is the dual role of electrowetting: it quantitatively increases the accessible active surface area and qualitatively enhances capacitance by facilitating the formation of Stern layer-dominated electric double layers. Furthermore, under conditions that promote sufficient electrowetting, multivalent ion charge carriers exhibit a stronger charge-neutralizing effect compared to monovalent ions, resulting in significantly enhanced specific capacitance. These results highlight the critical importance of multivalent charge carriers and mesopores, suggesting the need for targeted research to optimize these parameters for improved charge storage performance. This study offers a novel framework for advancing electrochemical systems beyond conventional strategies, such as increasing surface area or reducing ion-electrode distances.

Keywords: electrowetting, nanoporous carbon, supercapacitor, complex EDL, charge carrier

Supercapacitors are energy storage devices that store charge through the formation of an electric double layer (EDL) at the electrode-electrolyte interface.[1] Unlike batteries, which rely on ion diffusion and chemical reactions within bulk materials, supercapacitors store energy through the physical adsorption and desorption of ions on the electrode surface, enabling fast and reversible charge-discharge cycles.[2,3] However, this surface-based mechanism results in a limited energy density compared to rechargeable batteries.[4,5] To overcome this limitation, considerable efforts have focused on developing electrode materials with higher active surface areas and minimizing the ion-electrode distance to enhance EDL capacitance.[6-9]

Activated carbon (AC) is the most widely used electrode material for supercapacitors due to its exceptionally high specific surface area, high electrical conductivity, low cost, and well-established fabrication methods.[10] Despite these advantages, optimizing the EDL structure and understanding the dynamic ionic motion in AC-based systems—characterized by intricate microporous structures—remain significant challenges.[11,12] Experimental and theoretical studies have provided insights into the capacitive charge storage mechanisms within the nanopores of ACs.[13-18] Notably, nanopores with widths comparable to the Debye length exhibit unique phenomena, such as anomalous capacitance increases, overscreening, crowding, and nanoconfinement effects.[8,19-23] These observations highlight the confined EDL structure (compact layer) facilitates more effective charge screening compared to conventional extended EDL configurations (diffuse layer). Moreover, ion transport behaviors have been shown to depend strongly on pore geometry and ionophilicity.[12,23-25] For instance, the Grey research group proposed three simplified charge storage models—counter-ion adsorption, ion exchange, and co-ion desorption—to describe ionic motion during charging, providing a framework for understanding the complex charge storage mechanisms in nanostructured electrodes.[25-28] However, most of these studies are limited to results obtained using monovalent ions in micropore-sized pores (sub-nanometer to 2 nm).[13,15-18,21,25-27] There has been little systematic

comparison of the charge storage mechanisms when using mesopores and multivalent ions as charge carriers, compared to the conventional microporous AC and monovalent ion-based systems. Thus, further systematic studies are needed to fully elucidate the EDL behavior in nanoporous AC electrode systems, including the effects of pore size, charge carrier types, and their collective impact on supercapacitor performance.

Herein, we present an integrated experimental and theoretical investigation to explore the correlation between complex EDL structures in nanopores and their capacitance. To this end, AC samples with well-defined pore sizes of 1.4 nm (AC14) and 3.7 nm (AC37) were synthesized from pyroprotein precursors. The charge storage behavior was systematically examined using both monovalent cations (M^+) and divalent cations (M^{2+}), with sulfate anions dissolved in water to simplify the electrolyte composition. Capacitance was measured via cyclic voltammetry (CV) and galvanostatic methods, while inductively coupled plasma optical emission spectrometry (ICP-OES) quantified ion adsorption at open circuit potential (OCP) and charged states. Real-time electrode weight changes during voltage variations were tracked using electrochemical quartz crystal microbalance (EQCM) and correlated with ICP results. Molecular dynamics (MD) simulations with variable-pore-size nanopore models were employed to further analyze the charge storage behavior of M^+, M^{2+}, and SO_4^{2-} under OCP and charged conditions. This comprehensive approach offers novel insights into the effects of electrowetting and the interplay between pore size and charge carriers on capacitance, advancing our understanding of nanostructure-based complex EDL systems.

The nanopore size-tuned AC samples with similar morphologies, microstructures, and surface properties have been fabricated from silk-derived pyroprotein precursors through controlled chemical activation using different activation agents such as K_2CO_3 and KOH.[28-30] A detailed explanation of the fabrication method and the distinct characteristics of the resulting samples compared to commercial ACs is provided in Supplementary Note 1 and Figures S1–S5.[30] Field emission scanning electron microscopy (FE-SEM) images reveal that the AC14 and AC37 samples exhibit similar fibrous morphologies, distinctly different from the irregular morphology typically observed in commercial ACs (Figures 1a, 1b, and S4). To analyze the internal carbon microstructure, field emission transmission electron microscopy (FE-TEM) analysis was performed. The observed carbon microstructures were highly amorphous and complex, with no distinctive graphitic layers (Figure 1c, 1d, and S6). The FE-TEM images show that both samples exhibit similar structures, making it difficult to distinguish between their carbon microstructures. Further detailed graphitic microstructures are characterized by using X-ray diffraction (XRD) and Raman spectra. In the XRD patterns, a highly broad peak is observed in the two theta region of ~22º, indicating amorphous carbon structures with poorly ordered graphitic layers (Figure 1e). The lower angle intensities of the patterns are gradually increased with decreasing two theta. This is due to the presence of multitudinous nanopores in their carbon structures.[31] Raman spectra also reveal broad and fused *D* and *G* bands at ~1330 and ~1580 cm^{-1}, respectively (Figure 1f). The lateral domain size of the graphitic structures, L_a, is calculated from the deconvoluted Raman spectra (Figure S7), where the L_a values of the AC14 and AC37 samples are ~2.8 and ~2.5 nm, respectively. Hence, similar amorphous carbon structures with no distinctive microstructural characteristics have been observed in both samples.

Surface chemical structures of the AC14 and AC37 samples are analyzed through X-ray photoelectron spectroscopy (XPS). In the XPS C 1s spectra, the major aromatic carbon

structure is exhibited at 284.4 eV with a minor single bonding carbon structure centered at 285.1 eV (Figure 1g).[30,31] Also, C–O and C=O bonding peaks with relatively low intensities are detected at 286.4 and 288.5 eV, respectively, and the O 1s spectra support the presence of C–O and C=O functional groups in the carbon structures (Figure 1h).[30,31] C/O ratios of the AC14 and AC37 are ~15.4 and ~15.1, respectively, indicating that the similar contents of oxygen atoms are introduced in the product samples despite their different types of activation agent used.

Contrary to the similar microstructure and surface properties, the AC14 and AC37 have significantly different pore structures. In the nitrogen adsorption and desorption isotehm tests, the isotherm curves reveal highly different shapes in the relative pressure section of ≥ 0.1 (Figure 1i). The isotherm curve of the AC14 shows a nearly constant adsorption quantity with no hysteresis between adsorption and desorption curves, indicating poor pore-filling of additional nitrogen molecules after the initial mono/bi-layer nitrogen adsorption. This is a typical shape of microporous carbons which mainly have the small nanopores of ≤ 2 nm in diameter. In contrast, the isotherm curve of the AC37 exhibits continuous nitrogen adsorption in the wide range of relative pressure region between 0.02 and 0.65, and the following decrease in the curve slope in the higher relative pressure region of >0.65. Little hysteresis is observed in the end of the curve, which has a loop shape corresponding to H4 of the IUPAC classification.[32] This type of hysteresis loop is observed in the micro–mesopore size boundary. Also, the diagonal increase of adsorption quantity indicates a broad range of pore size distribution in a few nanometers. Pore size distribution data show their different pore structure more clearly (Figure 1j and S8). Most of the pore volume in AC14 are ranged below 2 nm, while those in AC37 are distributed between 2~5 nm. The peak point and average pore sizes are confirmed as 1.4 and 1.8 nm for AC14 and 3.7 and 3.5 nm for AC37, respectively. Additionally, micropore structures are characterized through CO_2 adsorption isotherm test at

273 K. The isotherm curves show a higher CO_2 adsoption quantity in AC14 than AC37, indicating more developed microporous structure in AC14 (Figure 1k). The pore size distribution data reveal that their pore size distributions are very similar but overall pore volume below 1 nm is higher in AC14 than AC37 (Figure 1l). Table S1 describes textural properties of the samples. Specific surface areas of AC14 and AC37 are 2,410 and 2,895 $m^2 g^{-1}$, respectively, which are the similar level each other. However, the micropore to mesopore surface area ratio (S_{mic}/S_{meso}) is significantly different as 11.05 and 0.06 for AC14 and AC37, respectively. This result proves that the pore structure is well-controlled as in a few nanometer sizes.

The electrochemical charge storage behaviors of AC14 and AC37 were investigated in various 0.5 M aqueous electrolyte systems (Na_2SO_4, K_2SO_4, $MgSO_4$, and $ZnSO_4$) within a three-electrode setup across a voltage window of –0.8 to 0.8 V vs. Ag/AgCl (charged states at 0.8 V, –0.8 V, and both are designated as +AC, –AC, and ±AC, respectively). In CV curves at a scan rate of 10 mV s^{-1}, AC14 displayed higher CV areas than AC37 in M^+-based electrolyte systems, suggesting that microporous structures with smaller nanopores (≤ 2 nm) store more charge through EDL formation (Figures 2a and 2b). Conversely, in multivalent cation (M^{2+})-based systems, AC37 exhibited larger CV areas and a more significant capacitance gap relative to AC14 (Figures 2c and 2d). These findings reveal that nanopore size and charge carrier type are crucial in determining EDL capacitances in nanoporous electrodes. Notably, capacitance trends remained consistent across positive and negative voltage ranges, despite identical anion carriers, emphasizing the dominant role of cations in shaping EDL structures in both electrodes. Galvanostatic testing at 1 A g^{-1} confirmed similar capacitance trends observed in the CV results (Figure S9), with bar graphs illustrating specific capacitance values across electrolyte systems (Figures 2e and 2f). These visualizations highlight that micropore-monovalent ion and mesopore-multivalent ion combinations yield higher capacitance (e.g., ±AC14–M^+ and

±AC37–M^{2+}), while opposite combinations result in lower capacitance (e.g., ±AC14–M^{2+} and ±AC37–M^{+}). Notably, the ±AC37–M^{2+} systems exhibit superior capacitance, approximately 237 F g^{-1}, compared to the 70–185 F g^{-1} observed in the other systems tested, highlighting the critical role of the mesopore-multivalent ion charge carrier combination.

To explore variations in specific capacitance across different pore size-charge carrier combinations, ex situ ICP-OES analysis was conducted on electrodes at OCP and charged states (see Experimental section). The ion concentration changes are shown in Figures 2g–l. At OCP, M^{+}-based systems exhibited significantly higher ion amounts than M^{2+}-based systems in both AC14 and AC37, highlighting differences in electrolyte wetting and electrochemically active surface area (Figures 2g and 2h). These data suggest that the active pore volume wetted by the electrolyte within the carbon electrode material can vary depending on the electrolyte system. Additionally, the quantities of anions and M^{2+} ions in AC37 were two to three times higher than those in AC14, indicating the advantage of larger pore sizes in facilitating the wetting and accommodation of anions and M^{2+} ions. In positively or negatively charged states, increased ion quantities compared with those in OCP states suggest ion insertion, while decreases imply ion egress. Strong dual-ion adsorption was noted in the high-capacitance systems like ±AC14–M^{+} and ±AC37–M^{2+} (Figures 2i–l). In contrast, the previously reported charge storage behaviors like counter-ion adsorption, co-ion desorption, and ion exchange were observed in the systems with lower capacitance, such as ±AC14–M^{2+} and ±AC37–M^{+} (Figures 2i–l). A noteworthy observation is that in the ±AC14–M^{+} system, which contained the higher amount of ions at OCP among the AC14-based systems, the highest quantity of ions was additionally inserted into the pores under applied voltage, surpassing all other systems in terms of total ion concentration (Figure S10). This result is particularly impressive considering that the pore volume of AC14 is less than half that of AC37 (Table S1). These findings suggest that a significant portion of the pores in the nanoporous carbon electrode remains inactive under

OCP conditions but becomes electrochemically active as voltage is applied, resulting in a substantial increase in active surface area. On the other hand, the –AC37–M^+ system, which was expected to contain the highest amount of ions due to its larger pore volume and smaller ion size, exhibited only negligible changes in ion concentration as voltage was applied. In the case of K^+, the behavior was even more pronounced, with co-ion desorption leading to an internal pore concentration lower than that observed at OCP. This indicates that the active surface area of carbon electrodes in the charged states is not solely determined by intrinsic properties such as specific surface area, pore volume, pore size, and the ionic radius of the charge carrier. Instead, it is influenced by a complex interplay of various factors.

In situ EQCM experiments for all the electrolyte systems further examined these unique charge storage behaviors (Figure 3). For a quantitative comparative analysis, the mass loading density of the AC14 and AC37 electrodes used in the EQCM tests was standardized to be identical. During a negative voltage sweep from 0.2 to –0.8 V vs. Ag/AgCl for the –AC14–M^+ and –AC37–M^{2+} systems, which exhibited the strong dual-ion adsorption, a rapid initial mass increase was observed (Figure 3a, 3b, 3g, and 3h). The mass change graphs reveal a linear mass increase and followed by logarithmic mass increase trend, which is similarly observed in the –AC14–M^+ and –AC37–M^{2+} systems. By dividing the entire voltage range into 0.2 V intervals and plotting the mass changes within each interval as a bar graph, it becomes evident that, in the –AC14–M^+ and –AC37–M^{2+} systems, the mass change in the initial range of 0.2 to –0.2 V vs. Ag/AgCl accounts for the majority of the total mass change (Figure 3i). In contrast, the –AC14–M^{2+} and –AC37–M^+ systems, which exhibited relatively lower capacitances, showed either a linear mass change across the entire voltage range or higher mass changes in the latter stages of the voltage sweep compared to the initial stages. Notably, the mass change values were significantly lower than those observed in the systems with higher capacitances. Specifically, the mass change in AC37–M^+ was approximately one-sixth to one-seventh of that

in AC14–M^+, which used the same charge carrier. Similarly, the mass change in AC14–M^{2+} was about one-third to one-fourth of that in AC37–M^{2+}.

Based on the experimental results obtained, the high-performance systems, ±AC14–M^+ and ±AC37–M^{2+}, share key characteristics: high specific capacitance, strong dual-ion adsorption, and similar EQCM mass-change behaviors. The enhanced capacitance is closely linked to the dual-ion adsorption behavior revealed by ICP-OES analysis and the substantial mass changes observed in EQCM measurements, indicating effective electrowetting within these systems.[33]

MD simulations were employed to investigate the distinctive charge storage mechanisms and the origins of the experimentally observed capacitance differences in nanoporous carbons. Cylindrical carbon nanopore models with systematically varied pore diameters (1, 2, 3, and 4 nm) were designed to represent the experimentally synthesized AC structures. These models immersed in 0.5 M aqueous solutions of K_2SO_4 (monovalent ions) and $MgSO_4$ (divalent ions) to study ion storage behavior (Figure 4a). Surface charges derived from experimental capacitance measurements were applied to simulate electrode polarization, allowing for the analysis of molecular distributions and dynamics within nanopores under applied positive and negative bias potentials.

Simulation results revealed significant variations in wetting behavior and ion corporation under electrically neutral conditions (Figure 4b, 4c and S11). For K_2SO_4, hydrophobic effects prevented both water (solvophobic) and ions (ionophobic) from entering 1 nm pores, while pores larger than 2 nm readily incorporated both water and ions, establishing 1 nm as the critical pore size for wetting and ion inclusion in monovalent electrolyte systems. In contrast, $MgSO_4$ systems demonstrated distinct behavior: while 1 nm pores exhibited similar solvophobic and ionophobic characteristics to those observed with K_2SO_4, 2 nm pores

permitted water molecule infiltration but remained ionophobic. Complete wetting and ion incorporation were achieved only in pores larger than 2 nm, identifying 2 nm as the critical pore size for divalent electrolyte systems. This ionophobicity of Mg^{2+} ions in 2 nm pores is attributed to their high hydration energy (–1830 kJ/mol compared to –295 kJ/mol for K^+, Figure S12) and larger hydration radius, which significantly increases the energetic cost of partial desolvation in confined pores. Consequently, the exclusion of Mg^{2+} ions also prevents SO_4^{2-} anion incorporation to maintain charge neutrality. These results highlight that the basic wetting properties of electrolytes in nanopores are collectively governed by both pore size and ion characteristics.

When charges were applied to the carbon atoms, significant changes in the equilibrium state of ions within the pores were observed under both positive and negative potentials. Notably, even in cases where wetting did not occur under neutral conditions—such as 1 nm pores in K_2SO_4 and 1 and 2 nm pores in $MgSO_4$—applying charges to the pores induced the inclusion of both water and ions (Figure 4d–f and S13). This directly demonstrates the electrowetting phenomenon observed in the experiments. The application of an electric potential lowers the energy barrier for electrolyte inclusion, enabling previously hydrophobic pores to incorporate electrolytes and consequently increasing the effective surface area for charge storage. As confirmed by ICP-OES and EQCM data, electrowetting increases the active surface area, promoting dual-ion adsorption and leading to a significant increase in capacitance. In $MgSO_4$ systems, the threshold pore size for electrowetting-induced ion incorporation remains larger compared to K_2SO_4, due to the stronger hydration shell of Mg^{2+} ions. This size-dependent electrowetting behavior explains why samples with smaller pore sizes (AC14) show limited capacitance with $MgSO_4$, while those with larger pores (AC37) exhibit enhanced capacitance through more effective electrowetting and ion incorporation. Notably, similar capacitance trends were observed under both positive and negative potentials, suggesting that

the charge storage mechanism is primarily governed by electrowetting and ion distribution patterns influenced by pore size and electrolyte properties, rather than being solely driven by SO_4^{2-} adsorption at positive potentials.

In pores smaller than the critical size for each electrolyte system (below 1 nm for K_2SO_4 and below 2 nm for $MgSO_4$), charge storage is dominated by electrowetting phenomena, where extreme spatial confinement induces partial desolvation of counter-ions as they enter the pore (Figure 4d). The reduction in effective ion size by partial desolvation allows ions to approach the pore walls more closely, minimizing the Stern layer thickness and maximizing EDL capacitance.[34,35] Monovalent cations such as K^+, with lower hydration energy and smaller hydration radii, undergo this desolvation process more readily, enabling their accessibility to smaller pores. In contrast, divalent cations like Mg^{2+}, with higher hydration energy, face significant energetic barriers to desolvation, requiring larger pores for incorporation. Within such confined nanopores, the EDL structure is primarily dominated by the Stern layer, as spatial constraints suppress the formation of a diffuse layer (Figure 4g). The strong spatial confinement and high ion concentration near the pore walls lead to densely packed counter-ions, in contrast to larger pores where both Stern and diffuse layers, composed of both cations and anions, contribute to capacitance.

In pores larger than the critical size, charge storage mechanisms shift to include ion exchange and co-ion desorption processes (Figure S13). The reduced spatial constraints allow greater mobility of both cations and anions for charge compensation. In divalent electrolytes, high charge density cations such as Mg^{2+} enhance capacitance through strong electrostatic interactions with the electrode surface. According to the Gouy-Chapman theory, the higher ionic strength of divalent ions increases space charge density, thereby enhancing capacitance.[36] These distinct pore size dependencies account for the observed capacitance variations across

different AC electrodes and electrolytes (Figure 4h). Maximum capacitance is achieved in the AC14–M^+ and AC37–M^{2+} systems, where electrowetting effectively enhances both the active surface area and Stern layer capacitance. These results highlight not only the quantitative impact of electrowetting on capacitance enhancement but also its qualitative effects. Furthermore, since the manifestation and degree of electrowetting are determined by the interplay between pore size and charge carrier type, this study underscores the critical importance of identifying pore size–charge carrier combinations that maximize electrowetting. This approach complements traditional strategies focused on increasing intrinsic surface area and reducing electrode-ion distance. Notably, in supercapacitor systems based on multivalent ions with high space charge density, maximizing electrowetting has the potential to achieve significant capacitance enhancements, demonstrating its substantial promise for advancing electrochemical energy storage.

In conclusion, the interplay between pore size, ion concentration, ion size and hydration energy, and spatial arrangement governs complex ionic behavior in nanopores. These factors collectively minimize the system's free energy in a given electric field through contributions from ion desolvation, electrostatic interactions, and entropic effects. The key findings of this study are as follows: (1) The significant gap between the specific surface area of AC electrodes and the active EDL surface area can be minimized through electrowetting. (2) The Stern layer-dominated EDL structures formed via electrowetting can qualitatively improve capacitance. Therefore, optimizing electrowetting with appropriate pore size and charge carrier combinations enables both the quantitative and qualitative enhancements of EDL capacitance. (3) Under sufficient electrowetting conditions, multivalent ion charge carriers exhibit higher capacitance than monovalent ions, with the combination of mesopores and multivalent ions showing the highest potential for capacitance enhancement. These insights suggest that optimizing electrowetting through the strategic design of nanopore size and electrolyte ions

can maximize capacitance, offering a novel approach beyond traditional strategies of increasing surface area or reducing ion-electrode distances.

Acknowledgements: This research was supported by the Basic Science Research Program through the National Research Foundation of Korea (NRF) funded by the Ministry of Education (RS-2023- 00302689).

Author contributions:

Conceptualization: E.L., H.-K.L., H.K., Y.S.Y.
Methodology: E.L., J.L., C.H.C., H.-K.L., H.K., Y.S.Y.
Investigation: E.L., M.M.K., B.S.Y., G.B., K.H.S., J.Y., S.M.L., H.S.P., Y.S.Y.
Visualization: E.L., J.L., D.H.K., J.C.H., C.Y.K., J.K.
Funding acquisition: C.H.C., H.K., Y.S.Y.
Project administration: Y.S.Y.
Supervision: H.-K.L., H.K., Y.S.Y.
Writing – original draft: E.L., H.-K.L., H.K., Y.S.Y.
Writing – review & editing: H.S.P., C.H.C., H.-J.J., H.-K.L., H.K., Y.S.Y.

Competing interests: Authors declare that they have no competing interests.

Data and materials availability: All data are available in the main text or the supplementary materials.

References

1. Conway, B. Electrochemical supercapacitors: Scientific fundamentals and technological applications (Kluwer, 1999).

2. Simon, P., Gogotsi, Y. & Dunn, B. Where do batteries end and supercapacitors begin? Science 343, 1210–1211 (2014).

3. Lukatskaya, M. R., Dunn, B., & Gogotsi, Y. Multidimensional materials and device architectures for future hybrid energy storage. Nat. Commun. 7, 12647 (2016).

4. Simon, P. & Gogotsi, Y. Perspectives for electrochemical capacitors and related devices. Nat. Mater. 19, 1151–1163 (2020).

5. Li, X. et al. High energy flexible supercapacitors formed via bottom-up infilling of gel electrolytes into thick porous electrodes. Nat. Commun. 9, 2578 (2018).

6. Yun, Y. S. et al. Microporous carbon nanoplates from regenerated silk proteins for supercapacitors. Adv. Mater. 25, 1993–1998 (2013).

7. Kim, N. R. et al. Amphicharge-storable pyropolymers containing multitiered nanopores. Adv. Energy Mater. 7, 1700629 (2017).

8. Chmiola, J. et al. Anomalous increase in carbon capacitance at pore sizes less than 1 nanometer. Science 313, 1760-1763 (2006).

9. Largeot, C. et al. Relation between the ion size and pore size for an electric double-layer capacitor. J. Am. Chem. Soc. 130, 2730-2731 (2008).

10. White, R. J., Budarin, V., Luque, R., Clark, J. H., & Macquarrie, D. J. Tuneable porous carbonaceous materials from renewable resources. Chem. Soc. Rev. 38, 3401-3418 (2009).

11. Wang, T. et al. Machine-learning-assisted material discovery of oxygen-rich highly porous carbon active materials for aqueous supercapacitors. Nat. Commun. 14, 4607 (2023).

12. Liu, X. et al. Structural disorder determines capacitance in nanoporous carbons. Science 384, 321–325 (2024).

13. Parejo-Tovar, A. et al. Operando tracking of ion population changes in the EDL electrode of a lithium-ion capacitor during its charge/discharge. Energy Storage Mater. 73, 103810 (2024).

14. Deschamps, M. et al. Exploring electrolyte organization in supercapacitor electrodes with solid-state NMR. Nat. Mater. 12, 351-358 (2013).

15. Feng, G., Qiao, R., Huang, J., Sumpter, B. G., & Meunier, V. Ion distribution in electrified micropores and its role in the anomalous enhancement of capacitance. ACS Nano 4, 2382-2390 (2010).

16. Rajput, N. N., Monk, J., & Hung, F. R. Ionic liquids confined in a realistic activated carbon model: A molecular simulation study. J. Phys. Chem. C. 118, 1540-1553 (2014).

17. Lyu, D. et al. Understanding sorption of aqueous electrolytes in porous carbon by NMR spectroscopy. J. Am. Chem. Soc. 146, 9897−9910 (2024).

18. Bazant, M. Z., Storey, B. D., & Kornyshev, A. A. Double layer in ionic liquids: Overscreening versus crowding. Phys. Rev. Lett. 106, 046102 (2011).

19. de Souza, J. P., Goodwin, Z. A. H., McEldrew, M., Kornyshev, A. A., & Bazant, M. Z. Interfacial layering in the electric double layer of ionic liquids. Phys. Rev. Lett. 125, 116001 (2020).

20. Prehal, C. et al. Quantification of ion confinement and desolvation in nanoporous carbon supercapacitors with modelling and in situ X-ray scattering. Nat. Energy 2, 16215 (2017).

21. Zheng, Y. et al. Significantly increased specific discharge capacitance at carbon fibers created via architected ultramicropores. J. Am. Chem. Soc. 146, 20291−20299 (2024).

22. Dvoyashkin, M., Leistenschneider, D., Evans, J. D., Sander, M., & Borchardt, L. Revealing the impact of hierarchical pore organization in supercapacitor electrodes by coupling ionic dynamics at micro- and macroscales. Adv. Energy Mater. 11, 2100700 (2021).

23. Kondrat, S., Wu, P., Qiao, R., & Kornyshev, A. A. Accelerating charging dynamics in subnanometre pores. Nat. Mater. 13, 387–393 (2014).

24. Wang, H. et al. In situ NMR spectroscopy of supercapacitors: Insight into the charge storage mechanism. J. Am. Chem. Soc. 135, 18968–18980 (2013).

25. Forse, A. C. et al. NMR study of ion dynamics and charge storage in ionic liquid supercapacitors. J. Am. Chem. Soc. 137, 7231-7242 (2015).

26. Forse, A. C., Merlet, C., Griffin, J. M., & Grey, C. P. New perspectives on the charging mechanisms of supercapacitors. J. Am. Chem. Soc. 138, 5731-5744 (2016).

27. Forse, A. C. et al. Direct observation of ion dynamics in supercapacitor electrodes using in situ diffusion NMR spectroscopy. Nat. Energy 2, 16216 (2017).

28. Hayashi, J., Horikawa, T., Takeda, I., Muroyama, K., & Ani, F. N. Preparing activated carbon from various nutshells by chemical activation with K_2CO_3. Carbon 40, 2381-2386 (2002).

29. Wang, J., & Kaskel, S. KOH activation of carbon-based materials for energy storage. J. Mater. Chem. 22, 23710-23725 (2012).

30. Cho, S. Y. et al. Carbonization of a stable β-sheet-rich silk protein into a pseudographitic pyroprotein. Nat. Commun. 6, 7145 (2015).

31. Moon, S., Lee, S. M., Lim, H. K., Jin, H. -J., & Yun, Y. S. Relationship between multivalent cation charge carriers and organic solvents on nanoporous carbons in 4 V-window magnesium ion supercapacitors. Adv. Energy Mater. 11, 2101054 (2021).

32. Thommes, M. et al. Physisorption of gases, with special reference to the evaluation of surface area and pore size distribution (IUPAC Technical Report). Pure Appl. Chem. 87, 1051-1069 (2015).

33. Wei, Z., Elliott, J. D., Papaderakis, A. A., Dryfe, R. A. W., & Carbone, P. Relation between double layer structure, capacitance, and surface tension in electrowetting of graphene and aqueous electrolytes. J. Am. Chem. Soc. 146, 760−772 (2024).

34. Qing, L. et al. Quantifying ion desolvation effects on capacitances of nanoporous electrodes with liquid electrolytes. Chem. Eng. Sci. 240, 116662 (2021).

35. Pean, C. et al. Confinement, desolvation, and electrosorption effects on the diffusion of ions in nanoporous carbon electrodes. J. Am. Chem. Soc. 137, 12627-12632 (2015).

36. Doblhoff-Dier, K. & Koper, M. T. Modeling the Gouy–Chapman diffuse capacitance with attractive ion–surface interaction. J. Phys. Chem. C 125, 16664-16673 (2021).

Figure Legends

Fig. 1 | Materials characteristics of AC14 and AC37. FE-SEM images of **a**, AC14 and **b**, AC37, and FE-TEM images of **c**, AC14 and **d**, AC37. **e**, XRD patterns, **f**, Raman spectra, XPS **g**, C 1s and **h**, O 1s spectra, **i**, nitrogen adsorption–desorption isotherms, **j**, pore size distribution derived from N_2 adsorption, **k**, carbon dioxide adsorption isotherms, and **l**, pore size distribution derived from CO_2 adsorption.

Fig. 2 | Electrochemical and ion concentration analysis of AC14 and AC37. CV curves of AC14 and AC37 obtained in 0.5 M **a**, Na_2SO_4, **b**, K_2SO_4, **c**, $MgSO_4$, and **d**, $ZnSO_4$ electrolytes at a sweep rate of 10 mV s^{-1} over a voltage window of –0.8 to 0.8 V vs. Ag/AgCl. Specific capacitance bar graphs for AC14 and AC37 in the voltage ranges of **e**, –0.8 to 0.2 V and **f**, 0.2 to 0.8 V. Ion concentrations at the OCP state in **g**, AC14 and **h**, AC37, and delta ion concentrations at charged states: **i**, –AC14 and **j**, +AC14, **k**, –AC37, and **l**, +AC37, obtained from ICP-OES analysis.

Fig. 3 | In situ EQCM characterization of AC14 and AC37 in various electrolyte systems. CV and mass variation curves of AC14 during voltage sweeps from 0.2 to –0.8 V in 0.5 M **a**, Na_2SO_4, **b**, K_2SO_4, **c**, $MgSO_4$, and **d**, $ZnSO_4$ electrolytes. CV and mass variation curves of AC37 during voltage sweeps from 0.2 to –0.8 V in 0.5 M **e**, Na_2SO_4, **f**, K_2SO_4, **g**, $MgSO_4$, and **h**, $ZnSO_4$ electrolytes. **i**, Total ion concentration bar graphs of AC14 and AC37 across different electrolytes.

Fig. 4 | Molecular dynamics analysis of pore size-dependent electrowetting and EDL structure evolution. a, Schematic illustration of the nanopore model system for MD simulations. **b,** Number of water molecules in nanopores of varying diameter under neutral conditions. **c,** Number of ions in nanopores under neutral conditions. **d,** Electrowetting behavior in confined nanopores and the difference between monovalent and divalent electrolytes. **e,** Number of ions in nanopores under negative potential. **f,** Number of ions in nanopores under positive potential. **g,** Cross-sectional ion density profiles showing EDL structure evolution with pore size. **h,** Schematic representation of the electrowetting-induced EDL capacity enhancement mechanism.

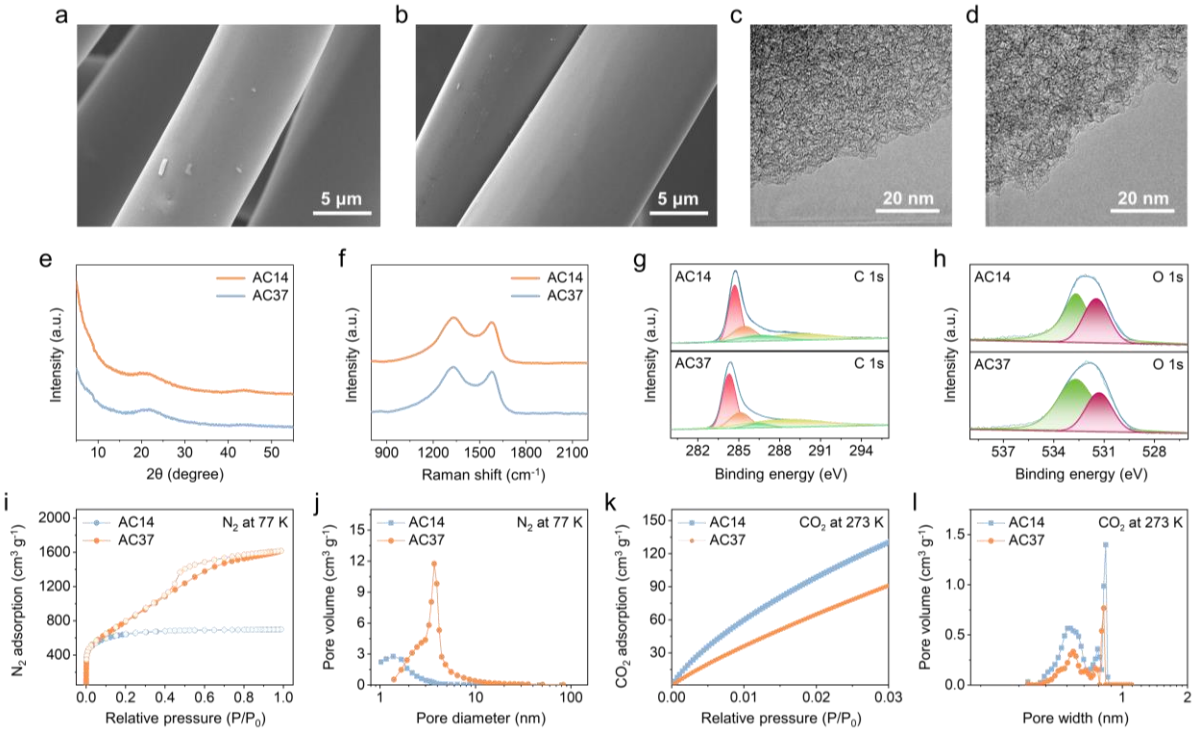
a
b
c
d
5 μm
5 μm
20 nm
20 nm
e
f
g
h
AC14
AC37
Intensity (a.u.)
2θ (degree)
Raman shift (cm⁻¹)
C 1s
O 1s
Binding energy (eV)
i
j
k
l
N2 adsorption (cm3 g-1)
Relative pressure (P/P0)
N2 at 77 K
Pore volume (cm3 g-1)
Pore diameter (nm)
CO2 adsorption (cm3 g-1)
CO2 at 273 K
Pore width (nm)

Fig. 1

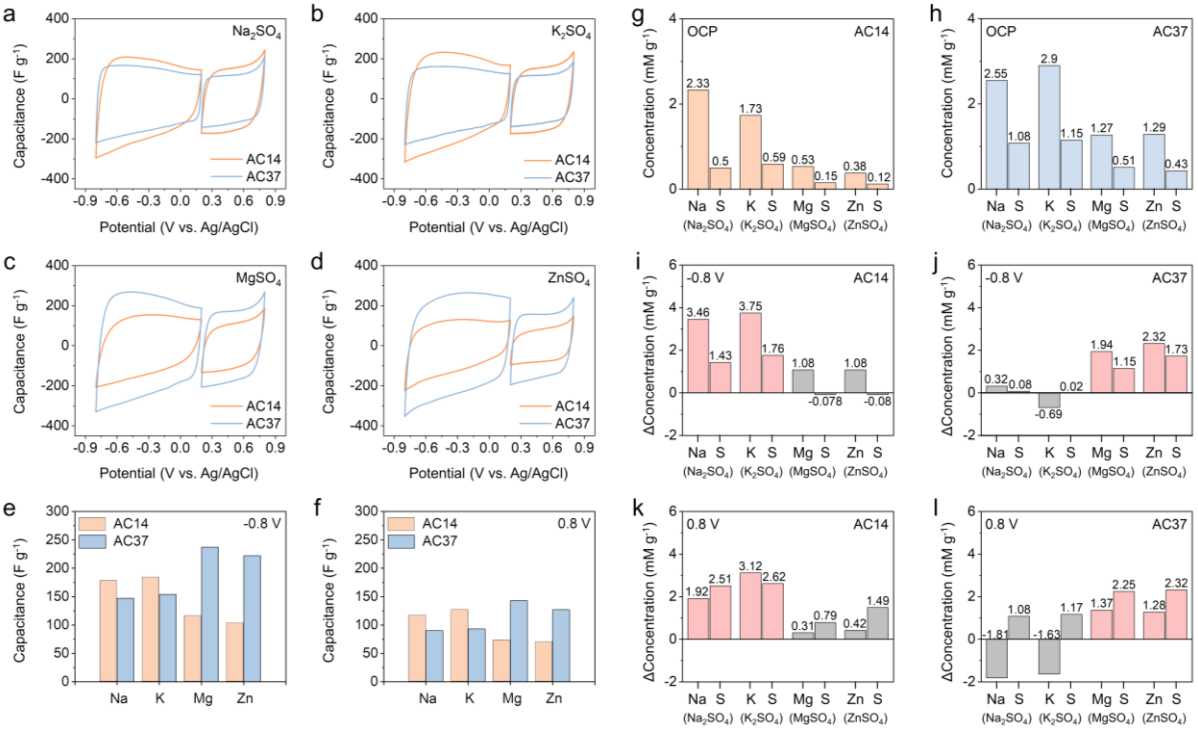
a
Na2SO4
AC14
AC37
Capacitance (F g-1)
Potential (V vs. Ag/AgCl)
b
K2SO4
c
MgSO4
d
ZnSO4
e
-0.8 V
f
0.8 V
Na
K
Mg
Zn
g
OCP
AC14
Concentration (mM g-1)
h
AC37
i
-0.8 V
ΔConcentration (mM g-1)
j
k
0.8 V
l
Na S K S Mg S Zn S
(Na2SO4) (K2SO4) (MgSO4) (ZnSO4)

Fig. 2

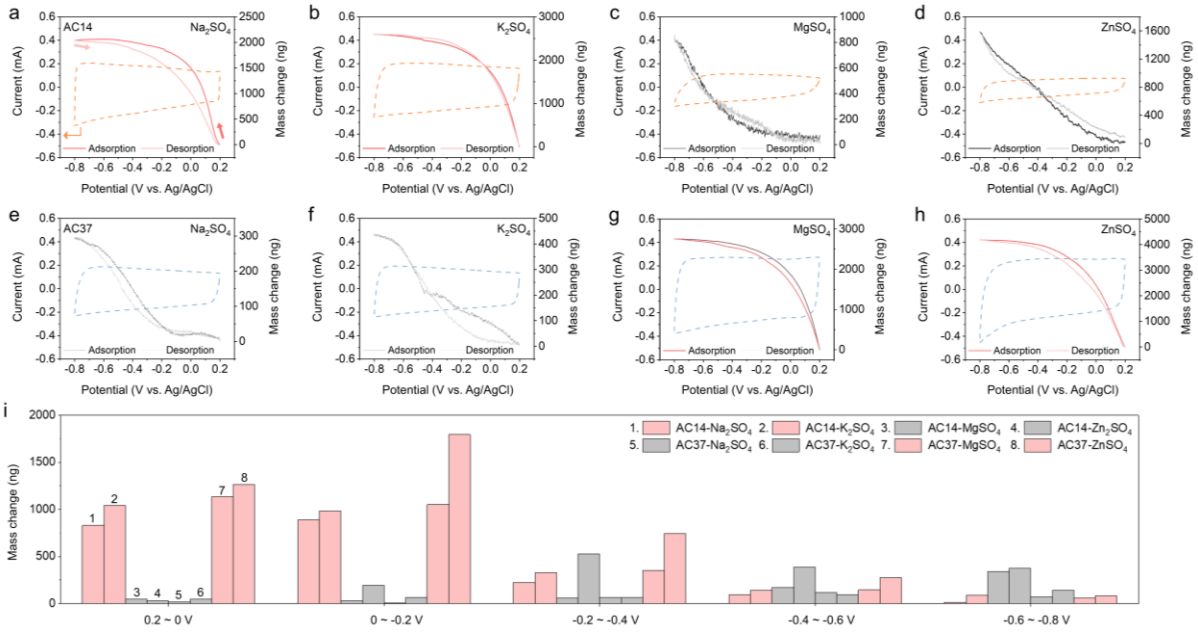
a
AC14
Na_2SO_4
b
K_2SO_4
c
$MgSO_4$
d
$ZnSO_4$
e
AC37
Na_2SO_4
f
K_2SO_4
g
$MgSO_4$
h
$ZnSO_4$
Current (mA)
Mass change (ng)
Potential (V vs. Ag/AgCl)
Adsorption
Desorption
i
Mass change (ng)
1. AC14-Na_2SO_4 2. AC14-K_2SO_4 3. AC14-$MgSO_4$ 4. AC14-Zn_2SO_4
5. AC37-Na_2SO_4 6. AC37-K_2SO_4 7. AC37-$MgSO_4$ 8. AC37-$ZnSO_4$
0.2 ~ 0 V
0 ~ -0.2 V
-0.2 ~ -0.4 V
-0.4 ~ -0.6 V
-0.6 ~ -0.8 V

Fig. 3

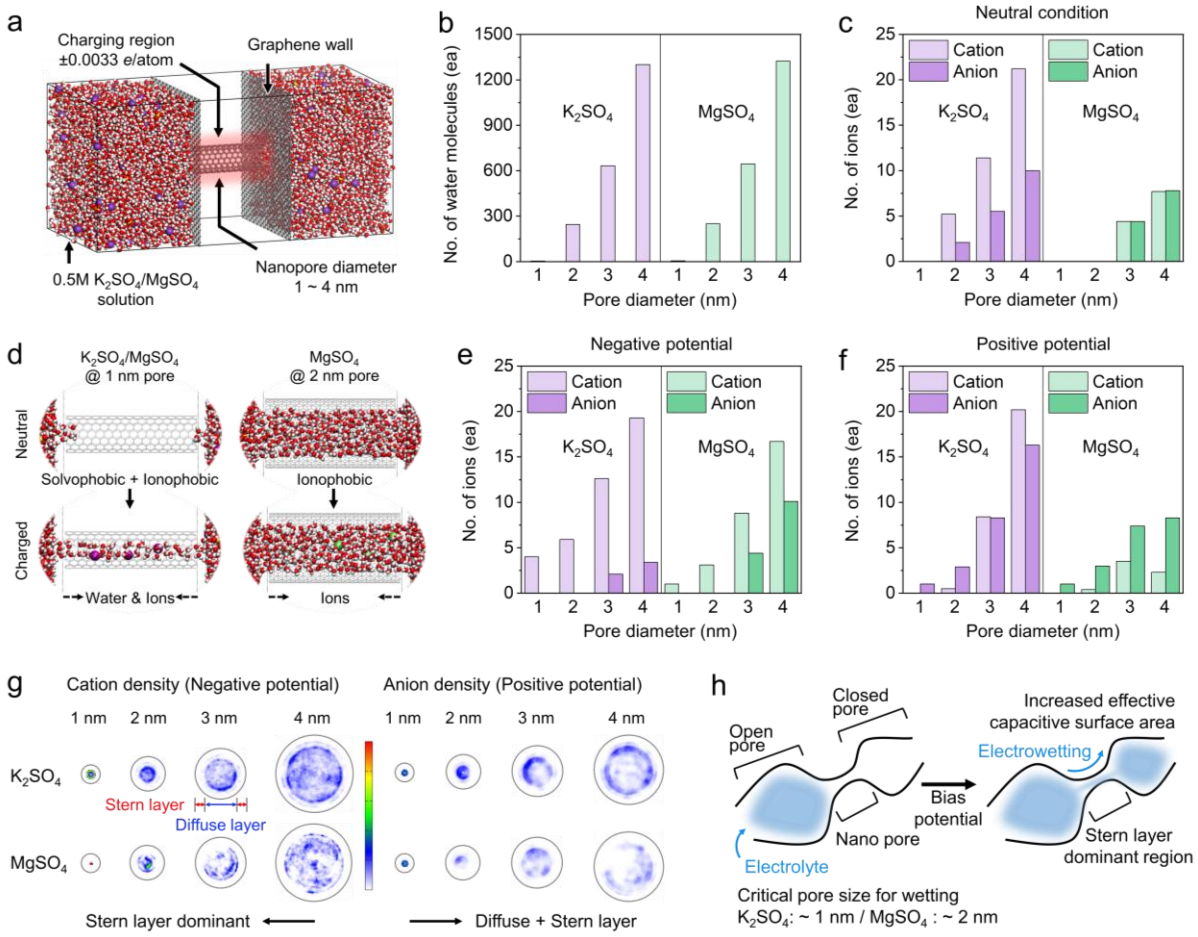
a
Charging region
±0.0033 e/atom
Graphene wall
0.5M K2SO4/MgSO4
solution
Nanopore diameter
1 ~ 4 nm
b
No. of water molecules (ea)
K2SO4
MgSO4
Pore diameter (nm)
c
Neutral condition
Cation
Anion
No. of ions (ea)
Pore diameter (nm)
d
K2SO4/MgSO4
@ 1 nm pore
MgSO4
@ 2 nm pore
Neutral
Charged
Solvophobic + Ionophobic
Ionophobic
Water & Ions
Ions
e
Negative potential
f
Positive potential
g
Cation density (Negative potential)
Anion density (Positive potential)
1 nm
2 nm
3 nm
4 nm
Stern layer
Diffuse layer
Stern layer dominant
Diffuse + Stern layer
h
Open pore
Closed pore
Increased effective
capacitive surface area
Electrowetting
Bias
potential
Nano pore
Electrolyte
Stern layer
dominant region
Critical pore size for wetting
K2SO4: ~ 1 nm / MgSO4 : ~ 2 nm

Fig. 4